Aftershocks of the 2012 M_w 8.6 Wharton Basin Intraplate Earthquake in the Eastern Indian Ocean Revealed by Near-Field Ocean-Bottom Seismometers

Laiyin Guo[1], Jian Lin[*1,2,3,4], Hongfeng Yang[5], and Jinyu Tian[1]

Abstract

The 11 April 2012 M_w 8.6 earthquake, the largest strike-slip earthquake recorded by instrument, occurred in the eastern Indian Ocean off the Sumatra subduction zone. During March–April 2017 and March–May 2018, two arrays of broadband ocean-bottom seismometers (OBSs) were deployed, respectively, near the epicentral area of the 2012 M_w 8.6 intraplate earthquake sequence. These were the first passive-source OBS experiments near the rupture region of the mainshock and subsequent aftershocks. A total of 1888 potential local events were detected through waveform matching, from which 164 events were subsequently located using the arrival time of the first *P* and *S* waves and were analyzed for hypocentral depth. The 2017 deployment was located close to the southern end of the mainshock and its largest aftershock (M_w 8.2). The events recorded in 2017 were found to be concentrated mostly along the intersection of two subfaults (F2 and F3) of the 8.6 earthquake, the rupture plane (F4) of the M_w 8.2 event, and over a broader region of complex fault structure in the Wharton basin. In contrast, the 2018 events were concentrated at two conjugate planes at the Ninetyeast ridge near the western end of a subfault (F3) of the M_w 8.6 mainshock. These results illustrate that the aftershocks of the 2012 strike-slip earthquakes have continued in 2017 and 2018. Furthermore, the 2017 and 2018 events were found to be concentrated at depth intervals of 0–10 and 20–30 km, respectively. The relatively small number of events at the intervening depth of 10–20 km was interpreted to be the result of the presence of a serpentinized layer in the uppermost mantle in the Wharton basin, which is consistent with the results of previous multichannel seismic studies in the region.

Cite this article as Guo, L., J. Lin, H. Yang, and J. Tian (2021). Aftershocks of the 2012 M_w 8.6 Wharton Basin Intraplate Earthquake in the Eastern Indian Ocean Revealed by Near-Field Ocean-Bottom Seismometers, *Seismol. Res. Lett.* **XX**, 1–13, doi: 10.1785/0220210096.

Introduction

On 11 April 2012, an M_w 8.6 earthquake occurred off the northwestern coast of northern Sumatra, which was the largest strike-slip earthquake in the oceanic plate of the Wharton basin. The mainshock was followed by the largest aftershock of M_w 8.2, which was approximately 150 km south of the mainshock (McGuire and Beroza, 2012). Those two events were located neither in the outer rise region controlled by plate flexure (Chen and Forsyth, 1978; Zhou *et al.*, 2015) nor were associated with large-scale deformation or hotspot volcanism; thus, they could be defined as "intraplate earthquakes" (Okal, 1983). The rupture process of the 2012 event imaged by back-projection method using seismic data from the Chinese, Japanese, and European seismic arrays, together with the aftershock distribution, demonstrated an extraordinarily complex multifault rupture lasting ~160 s (Meng *et al.*, 2012; Satriano *et al.*, 2012; Yue *et al.*, 2012; Ishii *et al.*, 2013, Zhao and Yao, 2018). Moreover, this was not the first time that an earthquake associated with more than one fault plane had been observed. For example, on 18 June 2000, the M_w 7.8 Wharton basin earthquake consisting of two subevents occurred on a pair of conjugate faults (Robinson *et al.*, 2001). Furthermore, the finite-fault models showed that the 2012 events rupture down to the upper mantle, reaching 60 km deep

1. Department of Ocean Science and Engineering, Southern University of Science and Technology, Shenzhen, China, https://orcid.org/0000-0002-4222-5449 (LG); 2. Department of Geology and Geophysics, Woods Hole Oceanographic Institution, Woods Hole, Massachusetts, U.S.A.; 3. Southern Marine Science and Engineering Guangdong Laboratory, Guangzhou, China; 4. Key Laboratory of Ocean and Marginal Sea Geology, South China Sea Institute of Oceanology, Chinese Academy of Sciences, Guangzhou, China; 5. Earth System Science Programme, Faculty of Science, The Chinese University of Hong Kong, Shatin, Hong Kong, China, https://orcid.org/0000-0002-5925-6487 (HY)

*Corresponding authors: jlin@whoi.edu

or more (Yue *et al.*, 2012; Wei *et al.*, 2013). It has been suggested by numerical studies that the rupture length of a fully developed strike-slip fault should be proportional to the brittle plate thickness (Weng and Yang, 2017).

Based on bathymetric and magnetic anomaly data, previous studies (e.g., Sandwell and Smith, 2009; Jacob *et al.*, 2014) have identified several distinct tectonic structures in the Wharton basin, including relict oceanic fracture zones. However, those structures' current activity levels are still poorly understood (Geersen *et al.*, 2015). Intraplate earthquakes, including strike-slip events in the Wharton basin, usually occur at distances greater than 600 km from coastlines. Moreover, permanent seismic stations are located primarily east of the Indian Ocean plate, along the northern Sumatra subduction zone. Because of the considerable distance of intraplate events from the seismic stations, it is difficult to obtain accurate locations of small events in the Wharton basin. Thus, near-source aftershock monitoring using ocean-bottom seismometers (OBS) will play a critical role in obtaining accurate hypocentral locations of aftershocks and examining the relations between seismicity and oceanic crustal structures in the Wharton basin.

To investigate the characteristics of the intraplate earthquakes and the diffuse plate boundary in the Wharton basin, we conducted OBS experiments in two periods in 2017 and 2018, respectively, and obtained detailed lateral and depth distributions of the seismicity. The experiments were located close to the 2012 M_w 8.6 and 8.2 earthquake rupture zones. This article describes the first near-field OBS observations in the Wharton basin following the 2012 intraplate earthquakes, reveals the relatively high-resolution location of the aftershock distribution, and explores the relation between the observed aftershocks and the shear zone structure determined from multibeam bathymetry (Singh *et al.*, 2017; Hananto *et al.*, 2018).

Data Acquisition

The OBS observations of the near-field aftershocks were conducted in two phases (Fig. 1). The first phase began on 13 March 2017, which was about five years after the 2012 mainshock in the Wharton basin. Six OBSs were deployed near the epicenter of the 2012 M_w 8.2 largest aftershock (92.463° E, 0.802° N). The deployment was conducted during a comprehensive oceanographic survey in the eastern Indian Ocean from the R/V Shiyan 3 of the South China Sea Institute of Oceanology. The OBSs were recovered on 11 and 12 April 2017. The second phase of the OBS deployment was conducted starting 26 March 2018, using seven OBSs. Five of the OBSs were deployed on the Ninetyeast ridge (NR), which was the northwestern termination of the subfault F3 of the 2012 mainshock (Wei *et al.*, 2013), and the other two OBSs were deployed east of the NR (Fig. 1). The OBS recovery was completed on 3 May 2018. The distances between the OBS stations were designed by considering a balance between obtaining good coverage of the 2012 earthquake sequences (Meng *et al.*, 2012; Yue *et al.*, 2012; Wei *et al.*, 2013; Hill *et al.*, 2015) and maintaining sufficient numbers of stations to record the signals of a common set of small events. One OBS instrument (Y09) at station OBS7 during the 2018 experiment was not recovered. The locations and observation periods of the OBSs are shown in Table 1.

Each OBS was equipped with a hydrophone and a three-component seismometer with the broadband range of 60 s to 50 Hz (Tian *et al.*, 2021). The sampling frequency of seismic signals was set to 100 Hz in the configuration files of the OBS. The OBS were deployed by free fall from the ship and the landing positions on the seafloor would be affected by ocean current. The intrument could drift 0.3 km or more at depths ranging from 1200 to 5400 m (Du *et al.*, 2018; Trabattoni *et al.*, 2019) without additional seafloor location information. The OBS positions on the seafloor, therefore, the Global Positioning System (GPS) position of the ship was used as a proxy for the OBS positions on the seafloor (Shinohara *et al.*, 2008). All of the OBSs recorded good-quality data, except OBS Y21 at station OBS3, whose clock-time drift was irregularly high during the 2017 deployment (Fig. A1). During the cumulative two-month deployment periods of the 2017 and 2018 experiments, a total of 15 teleseismic earthquakes of $M_w \geq 6$ were archived in the U.S. Geological Survey (USGS) catalog. However, no local earthquakes in the study area of the Wharton basin were reported in the USGS catalog.

Method

Time correction

The determination of earthquake locations depends strongly on the accurate timing of the OBS recordings (Gardner and Collins, 2012; Zhu *et al.*, 2019). In this study, GPS synchronization was available only before deployment or after recovery of the OBSs. During an OBS deployment period, the timing of the OBS was based on a high-quality temperature-compensated crystal oscillator (Gardner and Collins, 2012). Inaccurate temperature compensation and instrument ageing were the two largest potential sources for timing errors (Gardner and Collins, 2012). We calculated the ambient noise cross-correlation function (NCCF) signals between each OBS station pair to determine the time drifts, following the procedure of Tian *et al.* (2021). The relative time errors of two stations can be determined from the NCCF signals (Fig. A2), and we found that the total time errors were <40 ms for each station. Thus, we applied a linear-drift correction to the data by compensating for the average drift rate based on two synchronized GPS time stamps before and after the deployment (Geissler *et al.*, 2010; Le *et al.*, 2018; Liu *et al.*, 2018; Zhu *et al.*, 2020).

Earthquake detection and location

We adopted the method of waveform matching, which could successfully detect small earthquakes that would otherwise not be identifiable using conventional techniques (Peng and

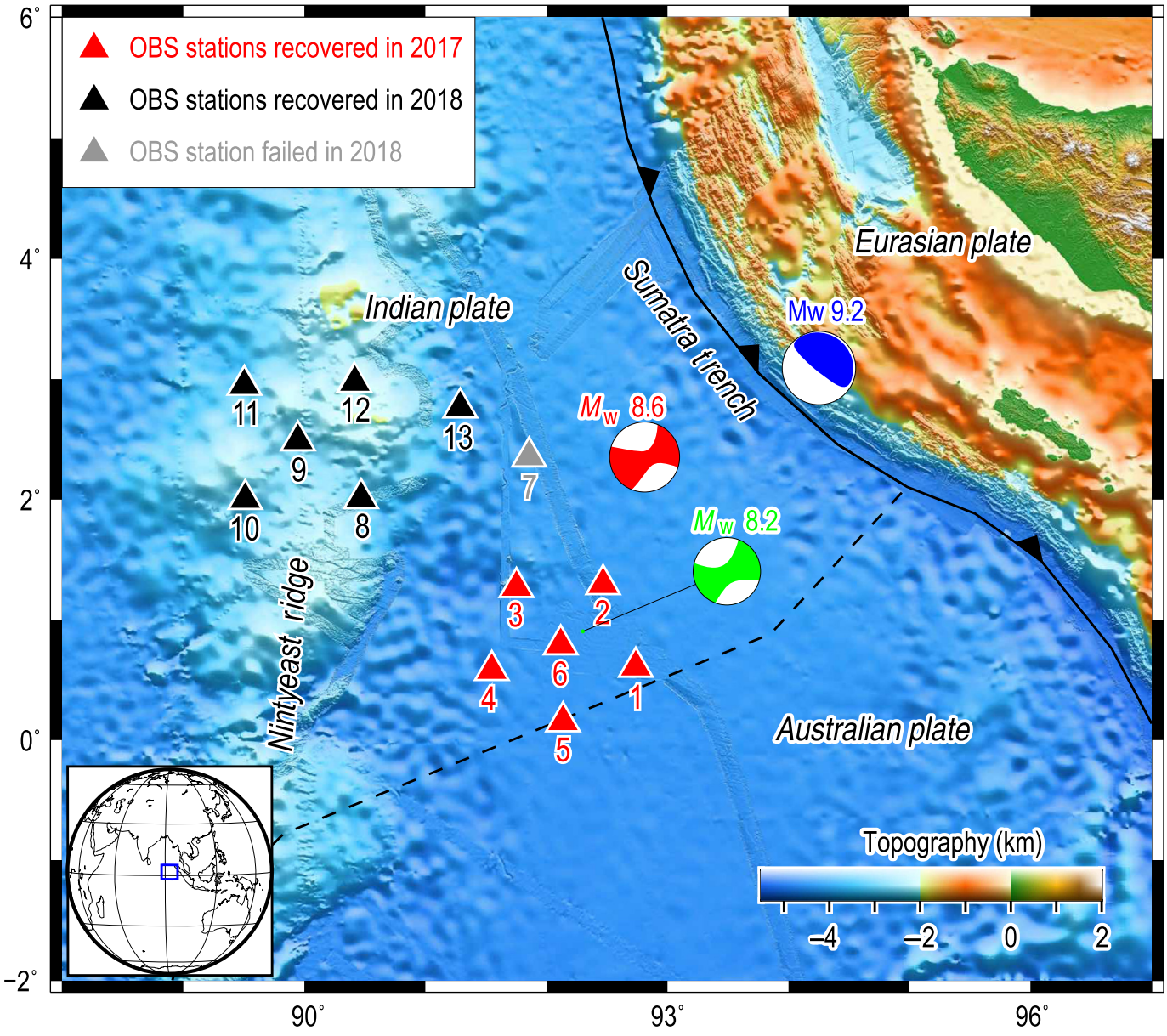

Figure 1. Location of ocean-bottom seismometer (OBS) stations (solid triangles) deployed in the Wharton basin. Blue focal mechanism plot shows the epicenter of the 2004 M_w 9.2 Sumatra megathrust earthquake. The red focal mechanism plot shows the 2012 M_w 8.6 intraplate event and the green focal mechanism plot shows its largest M_w 8.2 intraplate aftershock. Black solid lines with triangles mark the Sumatra subduction zone and black dashed lines show the hypothesized Indo-Australian plate boundary (Bird, 2003). Inset: Location of the study area (blue box). The color version of this figure is available only in the electronic edition.

Zhao, 2009; Yang *et al.*, 2009). The waveforms of the template events were used to search the continuous seismic waveform records observed by OBS network. A segment of a waveform with high similarity to the template event was then identified and considered to be a potential event similar to the template event. Three recording channels, that is, two horizontal components and one vertical component, of the OBS data were searched simultaneously to identify potential events and to reduce false detection (Zhu *et al.*, 2019). In general, local events reported in the catalog were employed as the templates. However, no local earthquakes were reported in the global catalog during the OBS deployment periods; we manually selected a 10-s-long segment of the waveform (OBS Y02) with distinctive body-wave arrivals and a high signal-to-noise ratio as a template earthquake (Fig. 2). To search for local earthquakes, we filtered both the template waveforms and the observed continous waveform records by a 2–8 Hz bandpass filter (Zhu *et al.*, 2019). We set the cross-correlation coefficient threshold value at 0.6, similar to that used in other studies (Zhu*et al.*, 2019, 2020; Chen *et al.*, 2021). After the first round of detection, we then used all detected earthquakes as templates and repeated the detection process once more.

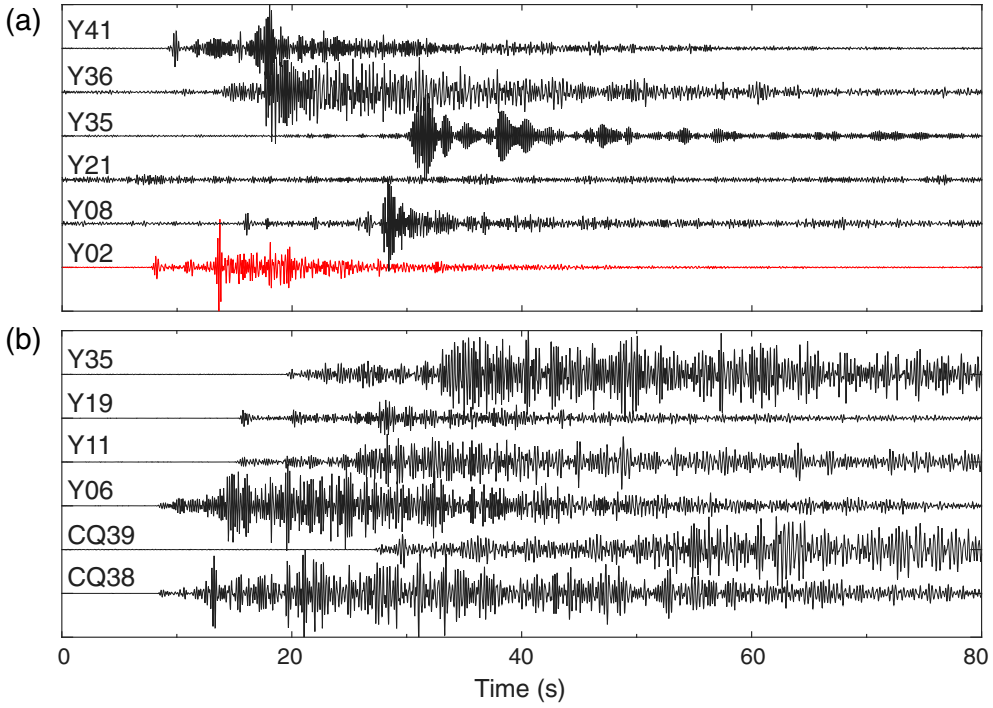

Figure 2. Example of seismograms of small earthquakes recorded by OBS during the (a) 2017 and (b) 2018 deployments, respectively. Vertical components are shown; a filter of 2–8 Hz was applied. A trace from OBS Y02 (red) was used as the template to detect potential events in this study. OBS names are labeled above each trace. The color version of this figure is available only in the electronic edition.

After the earthquake detection, we manually inspected the potiential events to keep true detections and picked *P*- and *S*-arrival times on three traces of the waveform recorded by OBS during the same period. The best-fit hypocentral locations were inverted using the Hypoinverse2000 software (Klein, 2002), a 1D velocity model, and *P*- and *S*-wave arrival times. In this study, we used a modified 1D preliminary reference Earth model velocity model (Fig. 3), in which the crustal thickness and velocity were represented by an oceanic crustal model extracted from the Crust 1.0 reference model for the study area (Laske *et al.*, 2013). Because the 2017 and the 2018 OBS networks were located at the plain seafloor and the high ridge, respectively, two different velocity models beneath these OBS networks were adopted in the earthquake location (Tables 2 and 3). We

TABLE 1
Locations and Operation Periods of Ocean-Bottom Seismometers (OBSs)

Station	OBS	Latitude (°N)	Longitude (°E)	Water Depth (m)	Operation Period
OBS1	Y41	0.6064	92.7371	4533	2017/03/13–2017/04/12
OBS2	Y02	1.2931	92.4673	4362	2017/03/13–2017/04/11
OBS3	Y21	1.2698	91.7515	3973	2017/03/16–2017/04/11
OBS4	Y35	0.5792	91.5482	4466	2017/03/16–2017/04/11
OBS5	Y08	0.1529	92.1364	4524	2017/03/13–2017/04/11
OBS6	Y36	0.7930	92.1168	4427	2017/03/16–2017/04/11
OBS7	Y09	2.3553	91.8560	4220	2018/03/28—Lost
OBS8	Y11	2.0088	90.4685	2966	2018/03/28–2018/05/02
OBS9	CQ38	2.4884	89.9464	2809	2018/03/27–2018/05/02
OBS10	Y06	2.0011	89.5109	2818	2018/03/27–2018/05/02
OBS11	Y19	2.9513	89.5032	3400	2018/03/27–2018/05/01
OBS12	Y35	2.9763	90.4122	2235	2018/03/27–2018/05/03
OBS13	CQ39	2.7623	91.2873	3978	2018/03/26–2018/05/03

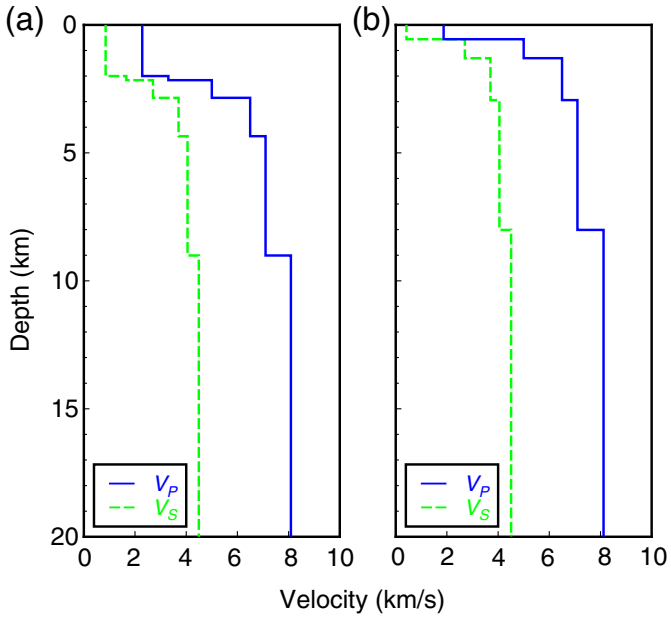

Figure 3. (a) Velocity structure models for the 2017 OBS network and (b) the 2018 OBS network for the hypocenter determinations using the preliminary reference Earth model, in which the crustal thickness and velocity were represented by an oceanic crustal model extracted from the Crust 1.0 reference model of the study area (Laske *et al.*, 2013). Blue-solid and green-dotted lines denote the *P*- and *S*-wave velocities, respectively. The color version of this figure is available only in the electronic edition.

also conducted station depth correction below different OBSs of the 2018 network during the location process. We did not further analyze the magnitudes of located events because determining earthquake magnitudes were not the goal of this study.

Results

Epicenter distribution

A total of 551 potential events were detected from the OBS data of the 2017 deployment through the waveform matching method as discribed earlier. A total of 130 events of relatively high certainty were identified after manual inspection to remove false detections. Then, we manually picked up *P* and *S* phases of the waveforms of the identified events. Ultimately, a total of 56 events were located. A total of 1337 potential events were first indentified from the 2018 OBS data, from which 108 events were similarly located. Histograms of the root mean square of the residual time errors for the 2017 and 2018 event location results are shown in Figure A3.

Our analysis shows that the majority of the located earthquakes occurred in the vicinity of the 2012 M_w 8.6 mainshock, the M_w 8.2 aftershock, and at the NR. A significant number of events also occurred over a broader region in the Wharton basin and the Sumatra subduction zone (Fig. 4a). The 2017 events were concentrated at the intersection between two subfaults (F2 and F3) of the 2012 M_w 8.6 mainshock and along approximately two-third length of the rupture plane (F4) of the 2012 M_w 8.2 largest aftershock. The 2018 events were concentrated at two conjugate belts at the western end of subfault (F3) of the 2012 M_w 8.6 mainshock near the NR (Fig. 4a).

The most apparent earthquake cluster trended N16°E along the 2012 M_w 8.2 rupture fault (F4, Fig. 4a); this cluster of the 2017 events was approximately 130 km long, between 0.2° N and 1.7° N. To the northwest of the 2017 cluster, another cluster of the 2018 events was located in the vicinity of 2.6° N; this cluster of events occurred in two belts of ~160 and 140 km long, trending N80°W and N9°E, respectively, at the western slope of the NR (Fig. 4a).

No events were reported in the Global Centroid Moment Tensor catalog or the USGS catalog during the OBS recording periods. Thus, our OBS experiments provided the most detailed near-field observations to illuminate the characteristics of aftershocks of the 2012 intraplate earthquakes in the Wharton basin.

Depth distribution of located aftershocks

Two vertical cross sections are shown in Figure 4, one with a strike of 2° N (AA′, Fig. 4c) and the other with a strike of 92.5° E (BB′, Fig. 4b). The distribution of earthquakes along the profile AA′ shows that there is one cluster of events near 90° E and one cluster near 92.5° E, respectively. The 2017 cluster of

TABLE 2
Velocity Model Used for the 2017 Earthquake Location

Layer	V_P (km/s)	V_S (km/s)	Thickness (km)
Sediments_1	2.28	0.85	2.00
Sediments_2	3.30	1.66	0.16
Crust_1	5.00	2.70	0.69
Crust_2	6.50	3.70	1.50
Crust_3	7.10	4.05	4.66
Uppermost mantle	8.09	4.49	

TABLE 3
Velocity Model Used for the 2018 Earthquake Location

Layer	V_P (km/s)	V_S (km/s)	Thickness (km)
Sediments_1	1.87	0.42	0.56
Crust_1	5.00	2.70	0.74
Crust_2	6.50	3.70	1.64
Crust_3	7.10	4.05	5.07
Uppermost mantle	8.12	4.51	

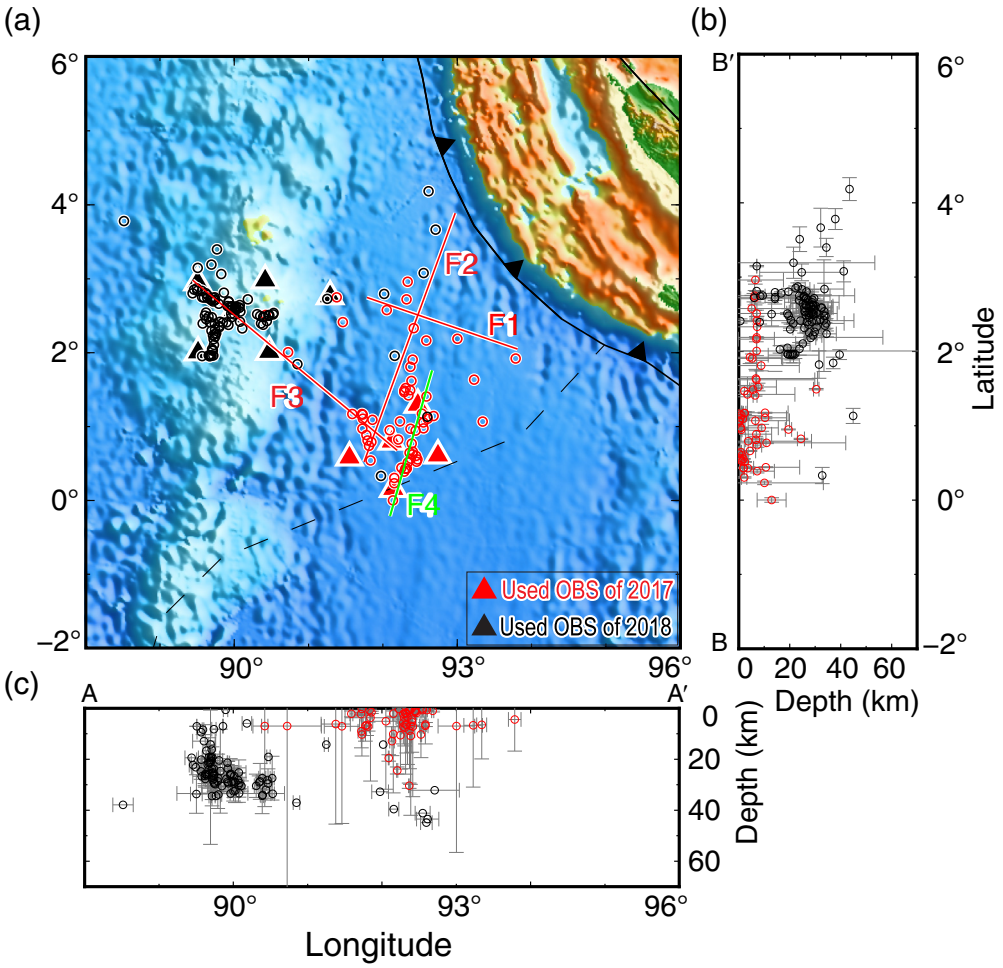

Figure 4. (a) Located hypocenter distribution of aftershocks recorded during the two deployment periods of 13 March–12 April 2017 (red circles) and 26 March–3 May 2018 (black circles), superimposed on bathymetry. (b) north–south and (c) west–east vertical cross sections. Calculated depth error bars are shown, except for events for which the hypocenter depths were fixed during inversion. The three red lines (F1–F3) indicate the subfaults of the 2012 M_w 8.6 earthquake whereas the green line indicates the rupture plane (F4) of the 2012 M_w 8.2 earthquake (Wei *et al.*, 2013). The color version of this figure is available only in the electronic edition.

events was concentrated at the relatively shallow depth of <10 km (red circles, Fig. 4c), whereas the 2018 cluster of events was concentered at depths of 20–35 km (black circles, Fig. 4c). Similarly, the depth differences between the 2017 and 2018 clusters are visible along the cross-sectional profile BB′ (Fig. 4b). The velocity model used in location process, phase picking, and clock drift might result in location errors. The average lateral and vertical errors of the 2017 earthquake location are 6 and 10 km, respectively, and the average lateral and vertical errors of the 2018 earthquake location are 14 and 5 km.

The depth distribution of the located earthquakes had distinctive characteristics (Fig. 5). We used a depth bin width of 5 km for counting the events. Approximately 18% of the events occurred within the upper 5 km, 37% within the upper 10 km, and 84% within the upper 30 km. The maximum number of events was clustered at depths of 5–10 and 25–30 km below the seafloor. The minimum number of events (11% of the total number of the located events) occurred at a depth of 10–20 km between the two peaks. The number of events decreased rapidly at depths greater than 30 km. In this study, no events were located in the Wharton basin at depths greater than 50 km.

Discussion

Aftershock lateral distribution and shear zones

Using surface-wave based analysis of the relative centroid locations, Chai *et al.* (2019) relocated 60 moderate-sized earthquakes ($4.7 \le M_w \le 7.2$) in a period of about four years following the 2012 events in the Wharton basin. Using the teleseismic double-difference method, Kwong *et al.* (2019) relocated 695 events in an area at 1° S–6° N and 88°–96° E during the period of January–December 2012. Arrays of events were recorded during our OBS experiments in the eastern Indian Ocean, revealing a much more detailed earthquake pattern than that obtained from land-based observation. Comparisons between the locations of the detected events in this study and those of Chai *et al.* (2019) and Kwong *et al.* (2019) are shown in Figure 6a,b, respectively. Even 5 or 6 yr after the 2012 earthquake, the seismicity pattern is consistent with the relocation of larger events of previous studies.

We projected the located earthquakes onto maps of the fracture zones and shear zones (Singh *et al.*, 2017; Hananto *et al.*, 2018), as determined from high-resolution multibeam bathymetry and seismic reflection data. There were two dominant trends of the geological structures in the study area: (1) the N70°W-striking right-lateral shear zones, and (2) the N20°E-striking left-lateral shear zones distributed among the nearly north–south-striking fracture zones and the NR, which were formed by N335°E-striking normal faults and N65°E-striking thrust faults (Hananto *et al.*, 2018). The distribution of the relocated

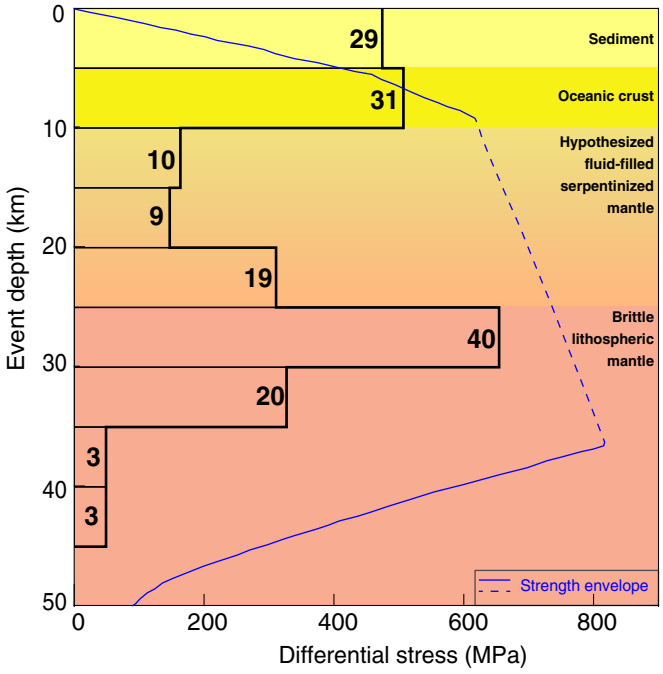

Figure 5. Depth distribution of located events, together with the number of recorded events for each depth interval. Also shown is the strength envelope (blue lines) for a model of 60 Ma oceanic lithosphere based on rheology of dry crust and mantle (Kohlstedt *et al.*, 1995). The upper layer (<10 km) is brittle with yield strength calculated assuming a friction coefficient of 0.6, meanwhile the yield strength of the lower layer (>35 km) is based on dry olive rheology; the brittle–ductile transition is zone is illustrated schematically by a dotted line. Background color stripes mark the sediment, crust, serpentinized mantle, and brittle lithospheric mantle layers, which Qin and Singh (2015) suggested based on a multichannel seismic study. The color version of this figure is available only in the electronic edition.

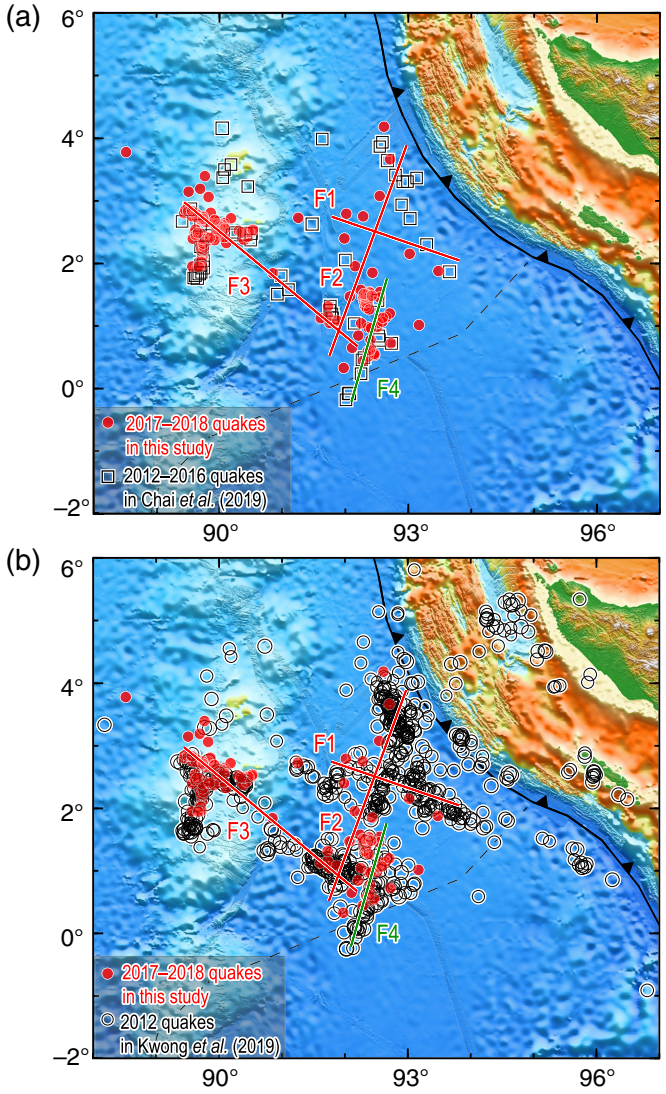

Figure 6. (a) Pattern of the located events (solid-red circles) in this study in comparison to the pattern of moderate-sized earthquakes that occurred in the Wharton basin during 2012–2016 (black squares, Chai *et al.*, 2019). (b) The pattern of the located events (solid-red circles) in comparison to earthquakes occurred in the Wharton basin in 2012 (black circles, Kwong *et al.*, 2019). The three red lines (F1–F3) indicate the subfaults of the 2012 M_w 8.6 earthquake, and the green line indicates the rupture plane (F4) of the 2012 M_w 8.2 earthquake (Wei *et al.*, 2013). The color version of this figure is available only in the electronic edition.

events is consistent with this deformation pattern, in which the lithospheric plate is filled by multiple short fault segments among fracture zones (Fig. 7a). Together with the reactivated fracture zones, these shear zones hosted the located earthquakes determined by the OBS observations (Fig. 7). So far, we have not seen a conjugate fault pair lying on the west end of the finite-fault model. As our model shows, there might be two conjugate faults (F5 and F6) cut off the NR (Fig. 8).

It was noted that these events did not align strictly along the shear zones or fracture zones on the local scale, illustrating the complex tectonics of a diffuse plate boundary. Chai *et al.* (2019) suggested that the unfocused nature of seismicity was due to the heterogeneity of the stress field.

In contrast to the relatively continuous fault length of a mature transform boundary, the 2012 M_w 8.6 mainshock occurred on a set of conjugate subfaults with relatively short lengths; the majority of the 2017 and 2018 events also occurred near these subfaults. This reflects the nature of a diffused plate boundary and complex tectonic deformation between the Australian and Indian plates (Gordon, 1998; Delescluse and Chamot-Rooke, 2007).

Although complex, the distribution of located aftershocks correlated with the Coulomb stress changes calculated from the 2012 M_w 8.2 finite-fault model. Along the rupture plane (F4) of the 2012 M_w 8.2 largest aftershock, the events observed in the 2017 experiment appear to correlate with areas of relatively small slip (Wei *et al.*, 2013; Fig. 9a) as well as with areas

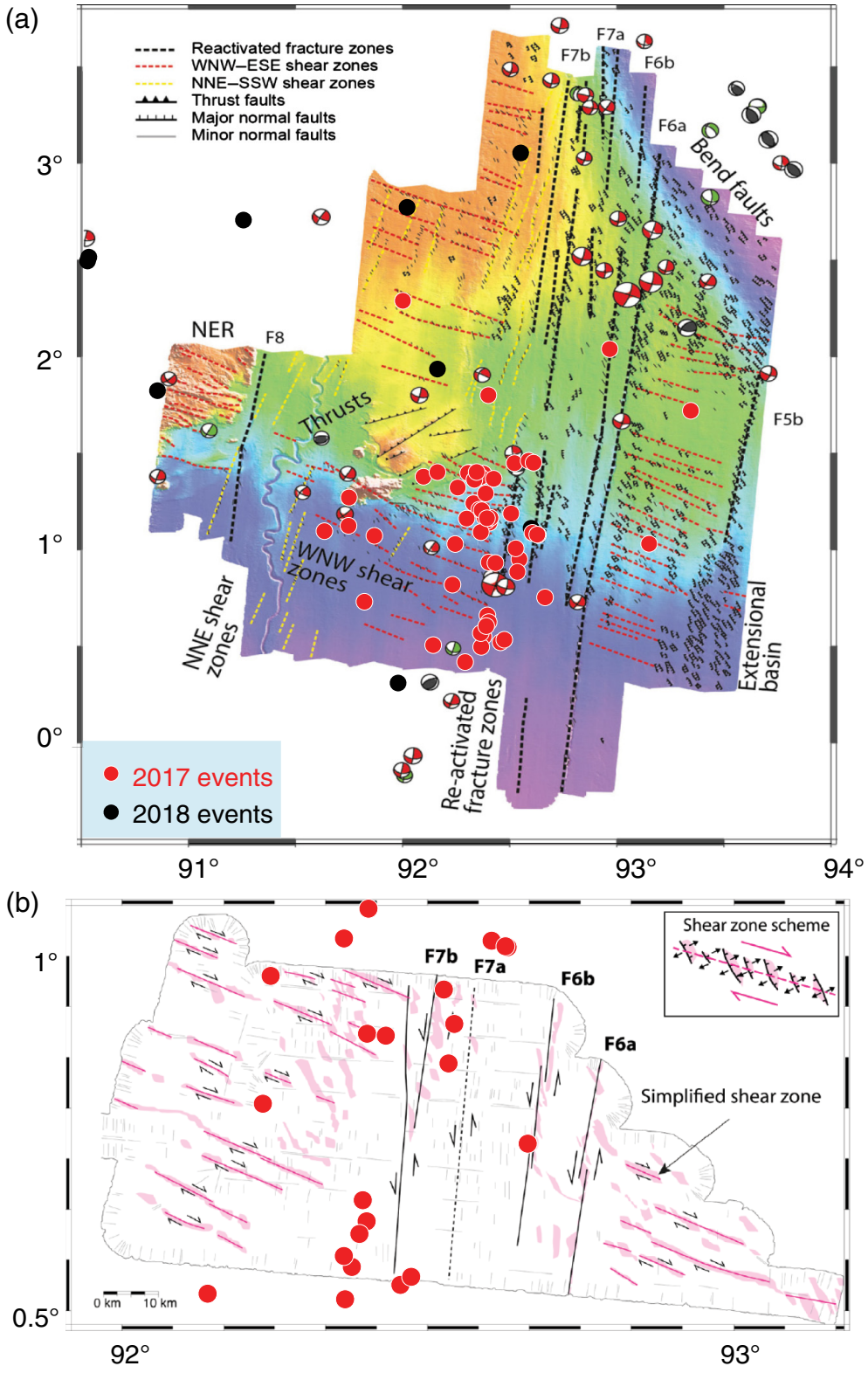

Figure 7. (a) Close view of the located 2017 events (solid-red circles) and 2018 events (solid-black circles) in the Wharton basin, superimposed on the multibeam bathymetry of the study area modified from Hananto *et al.* (2018). (b) The 2017 events superimposed on simplified interpreted geological structure of the study area modified from Singh *et al.* (2017). The inset shows a schematic shear zone (red lines). The color version of this figure is available only in the electronic edition.

of positive Coulomb stress change (assuming receiver faults with strike of 16, dip of 74, and rake of 0, the same as F4; Fig. 9b; Guo *et al.*, 2021).

Aftershock depth distribution and a hypothesized serpentinized layer

Kwong *et al.* (2019) further reported 74 relatively small events below the depth defined by the 600°C isotherm. They suggested that the 2012 mainshock ruptured through the entire oceanic lithosphere in the Wharton basin, penetrating below the seismogenic layer.

The depths of the located earthquakes were compared with a thermal model of the oceanic lithosphere (Fig. 10). The half-space cooling model assumed the thermal diffusivity of and mantle temperature at the 100 km depth to be 10^6 m^2/s and 1350°C, respectively (Parsons and Sclater, 1977). Our results showed that only 7 out of the 164 events were located at depths corresponding to a lithosphere temperature greater than 600°C; the maximum event depths corresponded to lithosphere temperature of 800°C. In comparison, aftershocks of the 2012 M_w 8.6 intraplate earthquake as deep as 55 km were reported, which exceeded the model depth of the 800°C isotherm (Kwong *et al.*, 2019). In addition, Aderhold and Abercrombie (2016) inferred that major aftershock in a broad region of the Wharton basin occurred within the depths of <40 km, with temperatures below 600°C. Molnar (2020) combined global observations and suggested that earthquakes can occur in

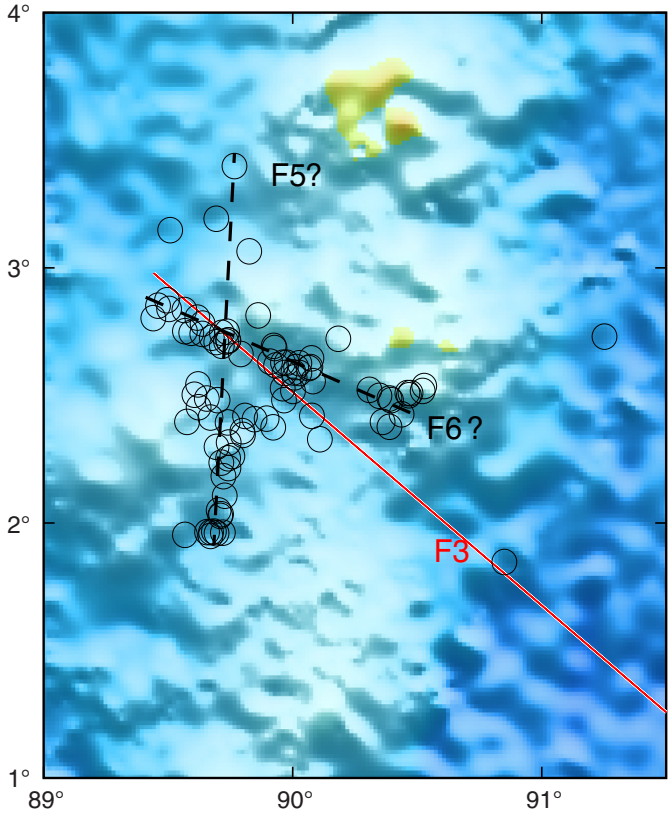

Figure 8. Zoom in of the area of 2018 located events. Black circles indicate the 2018 located events, and two black-dotted lines indicate hypothesis conjugate faults straddling the Ninetyeast ridge. The color version of this figure is available only in the electronic edition.

regions where mantle temperatures are greater than 600°C, even reaching 700°C–800°C.

Qin and Singh (2015) suggested that there was a fluid-filled serpentinized upper mantle layer above the brittle lithospheric mantle layer based on the number of faults and earthquakes. The number of located events was observed to decrease to a minimum at the depth interval of 10–20 km, which corresponds to the depth range of the hypothesized highly fluid-filled serpentinized layer (Fig. 5). The mantle peridotite could be serpentinized by the water penetrating along fault zone, which was produced by the bending related stresses combined with the stresses caused by diffuse deformation in the Wharton basin (Qin and Singh, 2015). The serpentinization was also an explanation for high heat flow in the Central Indian basin (Delescluse and Chamot-Rooke, 2008).

Investigation of intraplate seismicity is critical to advance our understanding of the nature of the diffuse plate boundary in the eastern Indian Ocean (Wiens *et al.*, 1985; Singh *et al.*, 2017; Hananto *et al.*, 2018). To further investigate the characteristics of microseismicity in the Wharton basin, we will revisit the 2017 and 2018 data set and determine the magnitudes of these events. Furthermore, we will carry seismic tomography in the future to further verify and quantify the degree of serpentinization (e.g., Zhu *et al.*, 2021) and derive the velocity structure beneath our OBSs.

Conclusions

This study introduced the first near-field OBS experiments conducted in the Wharton basin more than five years after the 2012 M_w 8.6 earthquake and presented the preliminary results. The method of waveform matching was employed to detect small local events from the OBS records. A total of 164 events were located using the Hypoinverse2000 method, yielding the following key results:

(1) The located events were distributed in a broad zone in the Wharton basin at the large scale, which was consistent with the diffused plate boundary. Meanwhile, some of these events exhibited a plausibly linear trend, such as along F4 of the 2012 M_w 8.2 and the conjugate faults of the 2012 M_w 8.6 near the western slope of the NR.

(2) The 2017 events at the eastern end of the study area were concentrated mainly at relatively shallow depths of <10 km. In contrast, the 2018 events near the NR were concentered at depths of 20–35 km. The lack of events at the intervening depth interval of 10–20 km was interpreted to indicate the presence of a serpentinized upper mantle layer, which is consistent with the results of prior multichannel seismic experiments in the Wharton basin.

Data and Resources

Seismic data used in this study were collected during the two passive-source ocean-bottom seismometers (OBSs) experiments in the Wharton basin. Data cannot yet be released to the public. Some figures in this study were made using the Generic Mapping Tools (Wessel and Smith, 1998). The Global Centroid Moment Tensor (Global CMT) catalog can be downloaded from http://www.globalcmt.org (last accessed on September 2020) and the events catalog used in this study comes from the U.S. Geological Survey (USGS) catalog (https://earthquake.usgs.gov/earthquakes/search, last accessed in September 2020).

Declaration of Competing Interests

The authors acknowledge that there are no conflicts of interest recorded.

Acknowledgments

The authors are grateful to Gaohua Zhu and Zeng Xin for technical assistance and to the captain and crew members of R/V Shiyan 3 for at-sea support during the 2017 and 2018 expeditions to the east Indian Ocean (NORC2017-10 and NORC2018-10). This article was supported by the Southern Marine Science and Engineering Guangdong Laboratory (Guangzhou) (GML2019ZD0205), National Natural Science Foundation of China (41890813, 41976066, 41976064, and 91628301), the Chinese Academy of Sciences (Y4SL021001, QYZDY-SSW-DQC005, 133244KYSB20180029, and 131551KYSB20200021), the National Key R&D Program of China (2018YFC0309800 and

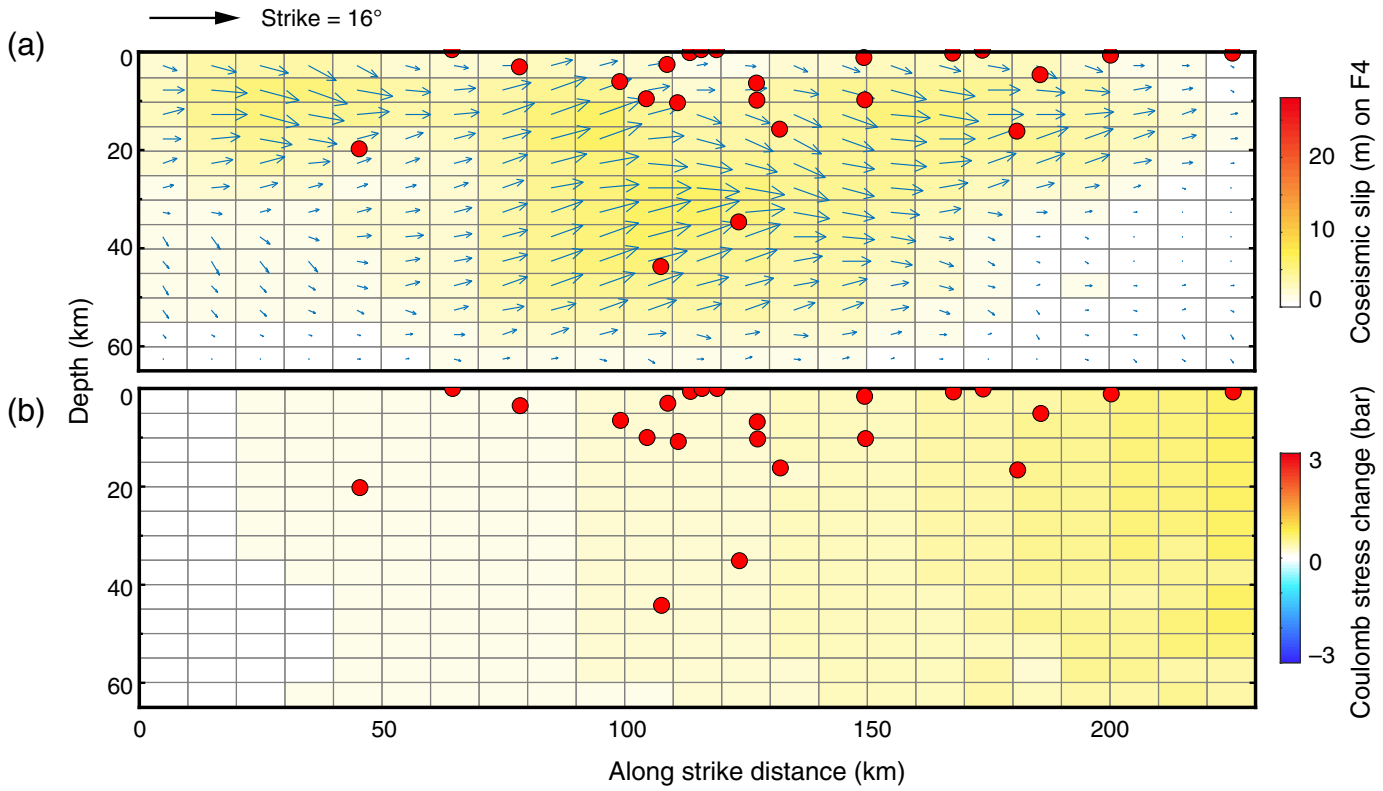

Figure 9. Located events projected on the rupture plane F4 of the M_w 8.2 earthquake. (a) The calculated coseismic slip on the F4. (b) Coulomb stress change on F4 caused by the M_w 8.2 earthquake on receiver faults (16°/74°/0°) as same as F4 (Guo *et al.*, 2021). The color version of this figure is available only in the electronic edition.

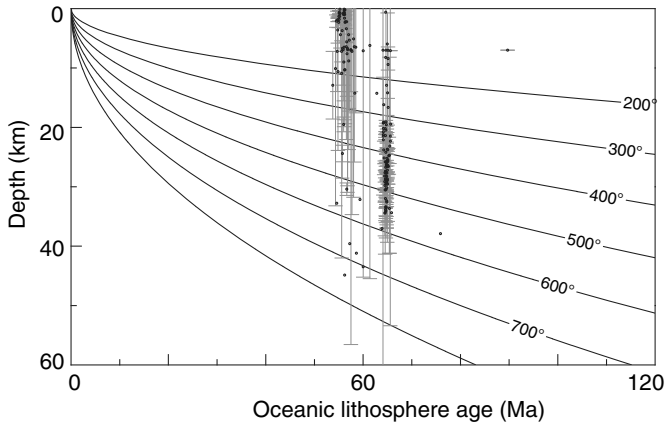

Figure 10. Located 2017 and 2018 intraplate events with vertical error bars (black circles) in the study area, superimposed on a half-space cooling model (Parsons and Sclater, 1977). Most of the events are located at depths with corresponding temperatures of less than 600°C.

2018YFC0310105), Hong Kong Research Grant Council (Grant Number 14304820), and the Guangdong Basic and Applied Basic Research Foundation (2021A1515012227).

References

Aderhold, K., and R. E. Abercrombie (2016). Seismotectonics of a diffuse plate boundary: Observations off the Sumatra-Andaman trench, *J. Geophys. Res.* **121,** no. 5, 3462–3478, doi: 10.1002/2015JB012721.

Bird,, P. (2003). An updated digital model of plate boundaries, *Geochem. Geophys. Geosys.* **4,** no. 3, doi: 1027 10.1029/2001gc000252.

Chai, C., C. J. Ammon, and K. M. Cleveland (2019). Aftershocks of the 2012 off-coast of Sumatra earthquake sequence, *Tectonophysics* **763,** 61–72, doi: 10.1016/j.tecto.2019.04.028.

Chen, H., X. He, H. Yang, and J. Zhang (2021). Fault-plane determination of the 4 January 2020 offshore pearl river delta earthquake and its implication for seismic hazard assessment, *Seismol. Res. Lett.* **92,** no. 3, 1913–1925, doi: 10.1785/0220200232.

Chen, T., and D. W. Forsyth (1978). A detailed study of two earthquakes seaward of the Tonga trench: Implications for mechanical behavior of the oceanic lithosphere, *J. Geophys. Res.* **83,** no. B10, 4995–5003, doi: 10.1029/jb083ib10p04995.

Delescluse, M., and N. Chamot-Rooke (2007). Instantaneous deformation and kinematics of the India-Australia plate, *Geophys. J. Int.* **168,** no. 2, 818–842, doi: 10.1111/j.1365-246X.2006.03181.x.

Delescluse, M., and N. Chamot-Rooke (2008). Serpentinization pulse in the actively deforming Central Indian basin, *Earth Planet. Sci. Lett.* **276,** nos. 1–2, 140–151, doi: 10.1016/j.epsl.2008.09.017.

Du, F., J. Zhang, F. Yang, M. Zhao, Q. Wang, and X. Qiu (2018). Combination of least square and Monte Carlo methods for

OBS relocation in 3D seismic survey near Bashi channel, *Mar. Geodes.* **41,** no. 5, 494–515, doi: 10.1080/01490419.2018.1479993.

Gardner, A. T., and J. A. Collins (2012). Advancements in high-performance timing for long term underwater experiments: A comparison of chip scale atomic clocks to traditional microprocessor-compensated crystal oscillators, in *OCEANS 2012 MTS/IEEE: Harnessing the Power of the Ocean*, IEEE, 1–8, doi: 10.1109/OCEANS.2012.6404847.

Geersen, J., J. M. Bull, L. C. McNeill, T. J. Henstock, C. Gaedicke, N. Chamot-Rooke, and M. Delescluse (2015). Pervasive deformation of an oceanic plate and relationship to large > Mw 8 intraplate earthquakes: The northern Wharton basin, Indian Ocean, *Geology* **43,** no. 4, 359–362, doi: 10.1130/G36446.1.

Geissler, W. H., L. Matias, D. Stich, F. Carrilho, W. Jokat, S. Monna, A. Ibenbrahim, F. Mancilla, M. A. Gutscher, V. Sallars, *et al.* (2010). Focal mechanisms for sub-crustal earthquakes in the Gulf of Cadiz from a dense OBS deployment, *Geophys. Res. Lett.* **37,** no. 18, doi: 10.1029/2010GL044289.

Gordon, R. G. (1998). The plate tectonic approximation: Plate nonrigidity, diffuse plate boundaries, and global plate reconstructions, *Annu. Rev. Earth Planet. Sci.* **26,** 615–642, doi: 10.1146/annurev.earth.26.1.615.

Guo, L., J. Lin, F. Zhang, and Z. Zhou (2021). Transfer of stress from the 2004 Mw9.2 Sumatra subduction earthquake promoted widespread seismicity and large strike-slip events in the Wharton basin, *Terra Nova* **33,** no. 1, doi: 10.1111/ter.12492.

Hananto, N., A. Boudarine, H. Carton, S. C. Singh, P. Avianto, J. Dyment, Y. Qin, D. Ghosal, R. Zuraida, P. E. Tapponnier, *et al.* (2018). Evidence of pervasive trans-tensional deformation in the northwestern Wharton basin in the 2012 earthquakes rupture area, *Earth Planet. Sci. Lett.* **502,** 174–186, doi: 10.1016/j.epsl.2018.09.007.

Hill, E. M., H. Yue, S. Barbot, T. Lay, P. Tapponnier, I. Hermawan, J. Hubbard, P. Banerjee, L. Feng, D. Natawidjaja, *et al.* (2015). The 2012 Mw 8.6 Wharton basin sequence: A cascade of great earthquakes generated by near-orthogonal, young, oceanic mantle faults, *J. Geophys. Res.* **120,** no. 5, 3723–3747, doi: 10.1002/2014JB011703.

Ishii, M., E. Kiser, and E. L. Geist (2013). Mw8.6 Sumatran earthquake of 11 April 2012: Rare seaward expression of oblique subduction, *Geology* **41,** no. 3, 319–322, doi: 10.1130/G33783.1.

Jacob, J., J. Dyment, and V. Yatheesh (2014). Revisiting the structure, age, and evolution of the Wharton basin to better understand subduction under Indonesia, *J. Geophys. Res.* **119,** no. 1, 169–190, doi: 10.1002/2013JB010285.

Klein, F. W. (2002). User's guide to HYPOINVERSE-2000, a Fortran program to solve for earthquake locations and magnitudes, *Report 2002-171*, U.S Dept. of the Interior, Geological Survey, Reston, Virginia.

Kohlstedt, D. L., B. Evans, and S. J. Machwell (1995). Strength of the lithosphere: Constraints imposed by laboratory experiments, *J. Geophys. Res.* **100,** no. B9, 845–848, doi: 10.1016/S0016-0032(16)90156-X.

Kwong, K. B., H. R. DeShon, J. Saul, and C. H. Thurber (2019). Constraining the oceanic lithosphere seismogenic zone using teleseismic relocations of the 2012 Wharton basin great earthquake sequence, *J. Geophys. Res.* **124,** no. 11, 11,938–11,950, doi: 10.1029/2019JB017549.

Laske, G., G. Masters, Z. Ma, and M. Pasyanos (2013). Update on CRUST1.0-A 1-degree global model of Earth's crust, in *EGU General Assembly 2013, EGU General Assembly* Vienna, Austria, 2658.

Le, B. M., T. Yang, Y. J. Chen, and H. Yao (2018). Correction of OBS clock errors using Scholte waves retrieved from cross-correlating hydrophone recordings, *Geophys. J. Int.* **212,** no. 2, 891–899, doi: 10.1093/gji/ggx449.

Liu, Y., C. Liu, C. Tao, H. Yao, L. Qiu, A. Wang, A. Ruan, H. Wang, J. Zhou, H. Li, *et al.* (2018). Time correction of the ocean bottom seismometers deployed at the southwest Indian ridge using ambient noise cross-correlation, *Acta Oceanol. Sin.* **37,** no. 5, 39–46, doi: 10.1007/s13131-018-1209-1.

McGuire, J. J., and G. C. Beroza (2012). A rogue earthquake off Sumatra, *Science* **336,** no. 6085, 1118–1119, doi: 10.1126/science.1223983.

Meng, L., J. P. Ampuero, J. Stock, Z. Duputel, Y. Luo, and V. C. Tsai (2012). Earthquake in a maze: Compressional rupture branching during the 2012 Mw8.6 Sumatra earthquake, *Science* **337,** no. 6095, 724–726, doi: 10.1126/science.1224030.

Molnar, P. (2020). The brittle-plastic transition, earthquakes, temperatures, and strain rates, *J. Geophys. Res.* **125,** no. 7, 1–24, doi: 10.1029/2019JB019335.

Okal, E. A. (1983). Oceanic intraplate seismicity, *Annu. Rev. Earth Planet. Sci.* **11,** no. 1, 195–214, doi: 10.1146/annurev.ea.11.050183.001211.

Parsons, B., and J. G. Sclater (1977). An analysis of the variation of ocean floor bathymetry and heat flow with age, *J. Geophys. Res.* **82,** no. 5, 803–827, doi: 10.1029/JB082i005p00803.

Peng, Z., and P. Zhao (2009). Migration of early aftershocks following the 2004 Parkfield earthquake, *Nature Geosci.* **2,** no. 12, 877–881, doi: 10.1038/ngeo697.

Qin, Y., and S. C. Singh (2015). Seismic evidence of a two-layer lithospheric deformation in the Indian Ocean, *Nat. Commun.* **6,** 1–12, doi: 10.1038/ncomms9298.

Robinson, D. P., C. Henry, S. Das, and J. H. Woodhouse (2001). Simultaneous rupture along two conjugate planes of the Wharton basin earthquake, *Science* **292,** no. 5519, 1145–1148, doi: 10.1126/science.1059395.

Sandwell, D. T., and W. H. F. Smith (2009). Global marine gravity from retracked Geosat and ERS-1 altimetry: Ridge segmentation versus spreading rate, *J. Geophys. Res.* **114,** B01411, doi: 10.1029/2008JB006008.

Satriano, C., E. Kiraly, P. Bernard, and J. P. Vilotte (2012). The 2012 Mw 8.6 Sumatra earthquake: Evidence of westward sequential seismic ruptures associated to the reactivation of a N-S ocean fabric, *Geophys. Res. Lett.* **39,** no. 15, doi: 10.1029/2012GL052387.

Shinohara, M., T. Kanazawa, T. Yamada, K. Nakahigashi, S. Sakai, R. Hino, Y. Murai, A. Yamazaki, K. Obana, Y. Ito, *et al.* (2008). Precise aftershock distribution of the 2007 Chuetsu-Oki earthquake obtained by using an ocean bottom seismometer network, *Earth Planets Space.* **60,** no. 11, 1121–1126, doi: 10.1186/BF03353147.

Singh, S. C., N. Hananto, Y. Qin, F. Leclerc, P. Avianto, P. E. Tapponnier, H. Carton, S. Wei, A. B. Nugroho, W. A. Gemilang, *et al.* (2017). The discovery of a conjugate system of faults in the Wharton basin intraplate deformation zone, *Sci. Adv.* **3,** no. 1, e1601689 , doi: 10.1126/sciadv.1601689.

Tian, J., J. Lin, F. Zhang, M. Xu, Y. Zhang, L. Guo, and X. Zeng (2021). Time correction of ocean-bottom seismometers using improved ambient noise cross correlation of multicomponents and dual-frequency bands, *Seismol. Res. Lett.* doi: 10.1785/0220200358.

Trabattoni, A., G. Barruol, R. Dreo, A. O. Boudraa, and F. R. Fontaine (2019). Orienting and locating ocean-bottom seismometers from ship noise analysis, *Geophys. J. Int.* **220,** no. 3, 1774–1790, doi: 10.1093/gji/ggz519.

Wei, S., D. Helmberger, and J. P. Avouac (2013). Modeling the 2012 Wharton basin earthquakes off-Sumatra: Complete lithospheric failure, *J. Geophys. Res.* **118,** no. 7, 3592–3609, doi: 10.1002/jgrb.50267.

Weng, H., and H. Yang (2017). Seismogenic width controls aspect ratios of earthquake ruptures, *Geophys. Res. Lett.* **44,** no 6, 2725–2732.

Wessel, P., and W. Smith (1998). New, improved version of generic mapping tools released, *Eos Trans. AGU* **79,** 579–579.

Wiens, D. A., C. DeMets, R. G. Gordon, S. Stein, D. Argus, J. F. Engeln, P. Lundgren, D. Quible, C. Stein, S. Weinstein, *et al.* (1985). A diffuse plate boundary model for Indian Ocean tectonics, *Geophys. Res. Lett.* **12,** no. 7, 429–432, doi: 10.1029/GL012i007p00429.

Yang, H., L. Zhu, and R. Chu (2009). Fault-plane determination of the 18 April 2008 Mount Carmel, Illinois, earthquake by detecting and relocating aftershocks, *Bull. Seismol. Soc. Am.* **99,** no. 6, 3413–3420, doi: 10.1785/0120090038.

Yue, H., T. Lay, and K. D. Koper (2012). En échelon and orthogonal fault ruptures of the 11 April 2012 great intraplate earthquakes, *Nature* **490,** no. 7419, 245–249, doi: 10.1038/nature11492.

Zhao, X., and Z. Yao (2018). The kinematic characteristics of the 2016 Mw7.8 offshore Sumatra, Indonesia earthquake, *Acta Geophys. Sin.* **61,** no. 3, 880–888, doi: 10.6038/cjg2018K0624.

Zhou, Z., J. Lin, M. D. Behn, and J. A. Olive (2015). Mechanism for normal faulting in the subducting plate at the Mariana trench, *Geophys. Res. Lett.* **42,** no. 11, 4309–4317, doi: 10.1002/2015GL063917.

Zhu, G., D. Wiens, H. Yang, J. Lin, M. Xu, and Q. You (2021). Upper mantle hydration indicated by decreased shear velocity near the southern Mariana trench from Rayleigh wave tomography, *Geophys. Res. Lett.* **48,** no. 15, doi: 10.1029/2021GL093309.

Zhu, G., H. Yang, J. Lin, and Q. You (2020). Determining the orientation of ocean-bottom seismometers on the seafloor and correcting for polarity flipping via polarization analysis and waveform modeling, *Seismol. Res. Lett.* **91,** no. 2, 814–825, doi: 10.1785/0220190239.

Zhu, G., H. Yang, J. Lin, Z. Zhou, M. Xu, J. Sun, and K. Wan (2019). Along-strike variation in slab geometry at the southern Mariana subduction zone revealed by seismicity through ocean bottom seismic experiments, *Geophys. J. Int.* **218,** no. 3, 2122–2135, doi: 10.1093/gji/ggz272.

Appendix

The appendix includes Figures A1–A3.

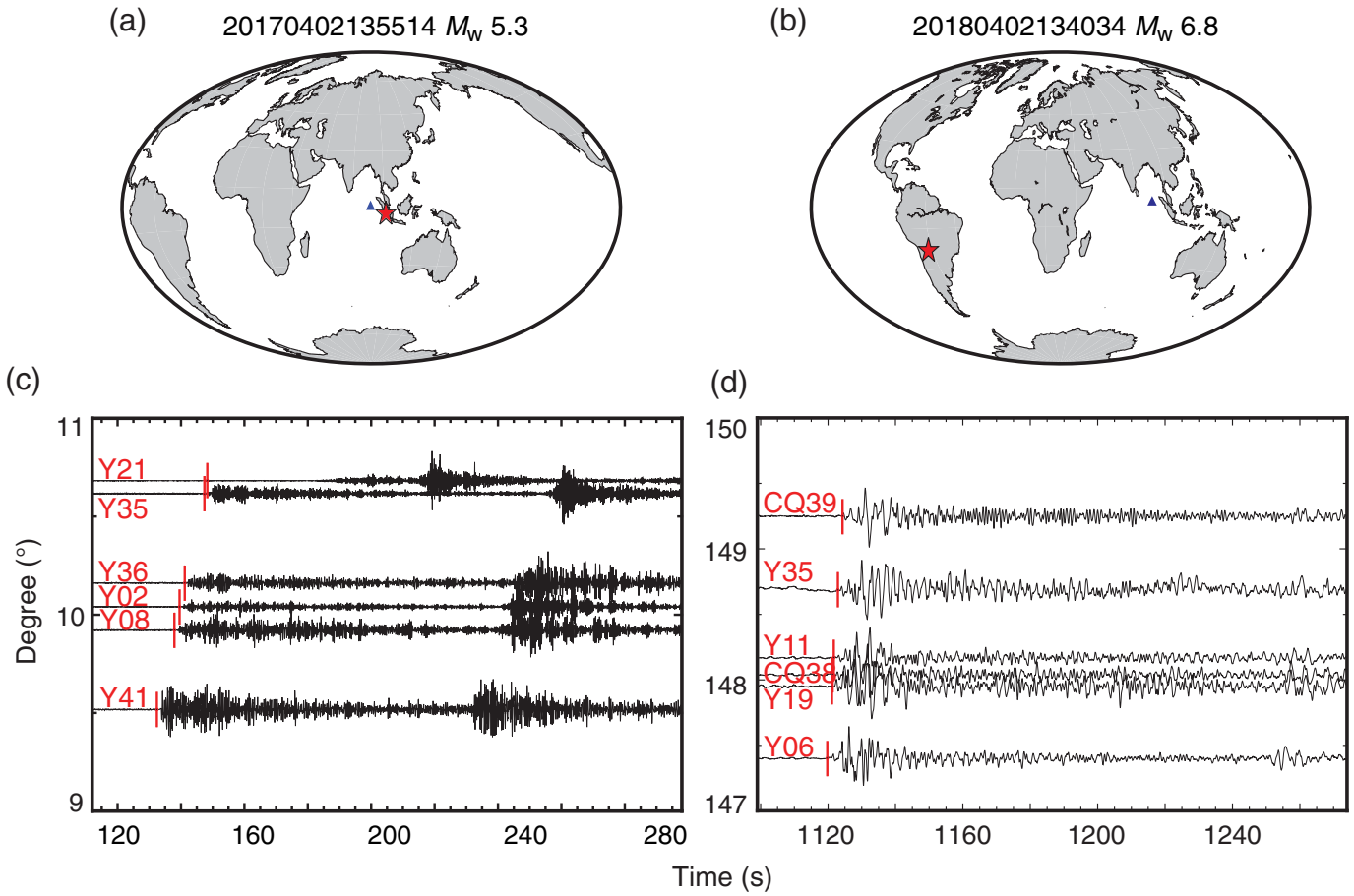

Figure A1. (a) Map showing the location of the ocean-bottom seismometer (OBS) cluster (blue triangle) and an M_w 5.3 earthquake (red star) during the deployment of OBSs in 2017, (c) waveforms aligned by the distances between the earthquake and stations. (b) Map showing location of the OBS cluster (blue triangle) and an M_w 6.8 earthquake (red star) during the deployment of OBSs in 2018, and (d) waveforms aligned by the distances between the earthquake and stations. OBS names are labeled in red at the beginning of the waveform profiles. Red lines indicate theoretical arrival times of (c) *P* waves and (d) *PKP* waves using the preliminary reference Earth model velocity model. The color version of this figure is available only in the electronic edition.

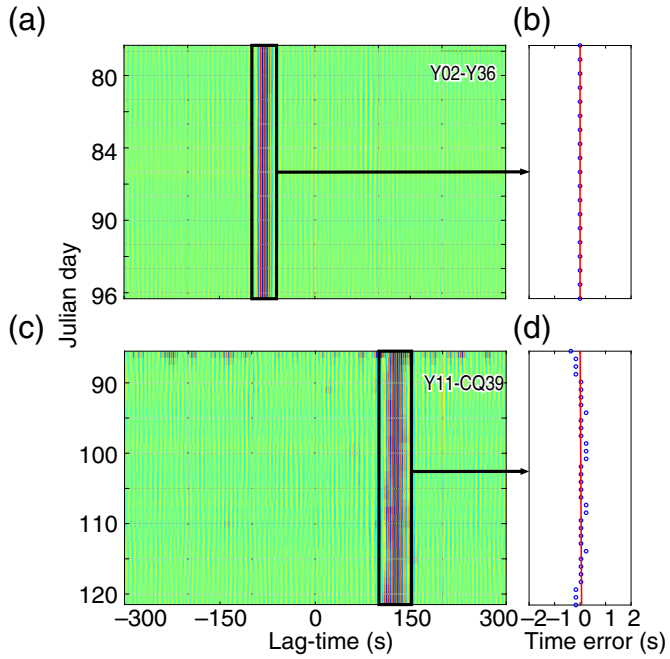

Figure A2. Examples of OBS time error detection. Noise cross-correlation function signals from hydrophone recordings at (a) Y02–Y36 and (c) Y11–Q39 pairs. Relative OBS time errors of (b) Y02Y36 and (d) Y11CQ39. The color version of this figure is available only in the electronic edition.

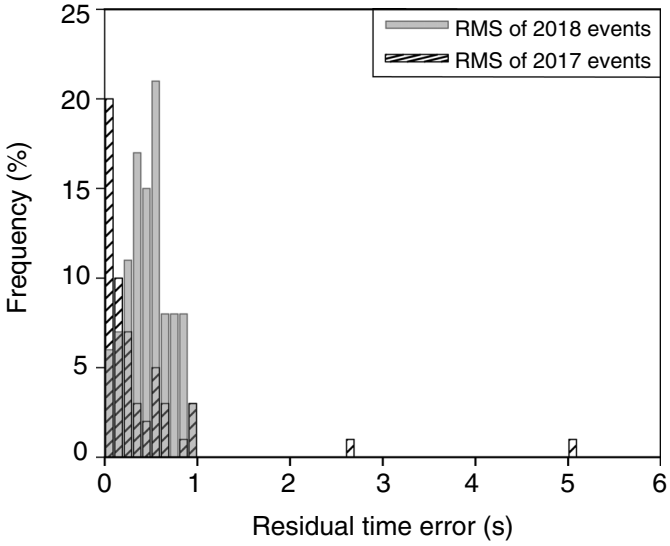

Figure A3. Histograms of root mean square of the residual time errors for the best-fit location models of the 2017 events (filled with diagonal stripes) and 2018 events (filled with gray shade).

Manuscript received 9 April 2021
Published online 22 December 2021